Application of diffractive optical elements in confocal microscopy

Zheng Li

Vision and Fusion Laboratory
Institute for Anthropomatics
Karlsruhe Institute of Technology (KIT), Germany
zheng.li@kit.edu

Technical Report IES-2018-03

Abstract

In traditional confocal microscopy, there is a tradeoff between the spatial resolution and the field of view due to the limitations of the objective lenses. To solve this problem, diffractive optical elements (DOEs) are used to generate illumination spots with high NA in a large area simultaneously. However, such DOEs in current research are only used as illuminators. In this work, the idea of superposition is utilized in DOEs to have flexible functionality and replace high-NA objectives for confocal measurement. To design the DOEs, different numerical simulation methods for light propagation are investigated and compared. Rayleigh-Sommerfeld integral is chosen to simulate the DOEs to get accurate results. Two kinds of DOEs are designed and simulated for 3D confocal surface measurements.

1 Introduction

Confocal microscopy has long become the golden standard in life sciences and other fields [VBR+15]. In a simple single-spot laser scanning confocal microscope, a very focused spot is produced by an objective to illuminate a tiny part of the object. The bright spot on the object is again imaged by the objective onto the image sensor. A pinhole is used to block out-of-focus light scattered by the object to have a sharper image of the spot on the object. In this way, much better

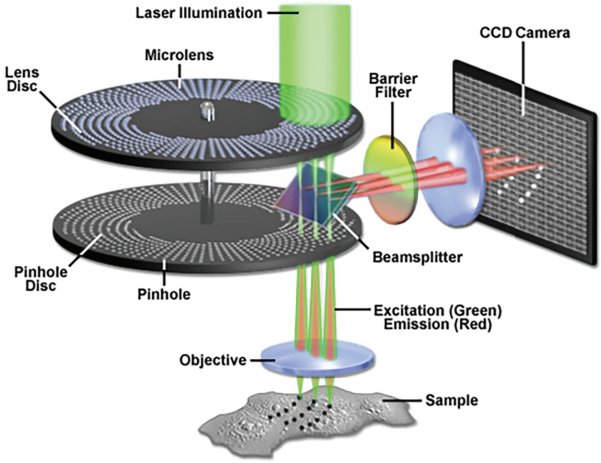

Figure 1.1: Optical configuration of a spinning disk microscope [DSS+09].

axial resolution than wide-field microscopy can be achieved and 3D images of the object can be obtained through layer-by-layer scanning. Furthermore, a multi-spot array can be used to increase the scanning speed. For example, Fig. 1.1 shows a Nipkow spinning disk which produces multiple spots to faster scan the sample.

One of the key components in a confocal microscope is the objective. The resolution of the microscope is directly related to the produced spot size, and the spot size is determined by the numerical aperture of the objective. The numerical aperture is defined as in Eq. (1.1), where n is the refractive index of the medium in which the objective works and θ is the half angle of the light cone which the objective can collect.

$$\mathrm{NA} = n \sin\theta \tag{1.1}$$

High-NA objectives provide better resolution. However, high-NA objectives with large diameters, e.g. lithography lenses, are very difficult and expensive to design and produce, which makes them impractical for microscopic applications [Zhe16]. Objectives need to get closer to the sample with the increase of NA. This leads to a limited field of view, which means only a small portion of the sample can be scanned at once. Besides, due to the complex structures of high-NA lenses, they are also very expensive.

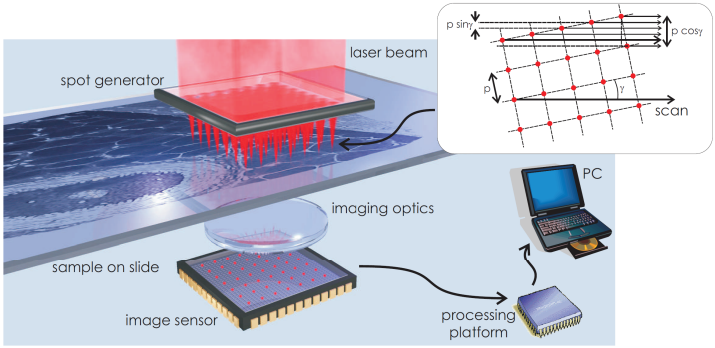

Figure 1.2: Optical configuration of a multi-spot scanning microscope using a DOE [HVS12].

In order to solve these problems, using DOEs as array illuminators has been proposed to scan large-area samples with comparable resolution to the standard confocal microscopy [HVS12][LSB12][LB14].

Fig. 1.2 shows the principle of a multi-spot scanning microscope based on a DOE illuminator. In this case, the DOE acts as an array of Fresnel lenses with overlapping apertures. It focuses plane wave into tiny illumination spots. A complete image of the sample is obtained by scanning it with the spot array. The array is placed at an angle to the scanning direction which allows one-axis scanning for a 2D plane.

However, such DOEs are not suitable for measuring 3D surfaces of opaque samples, because the spots cannot be imaged from the same side through the DOEs. So the imaging systems must be placed on the opposite sides of the DOEs and only transparent or semi-transparent samples can be measured. In order to avoid this limitation, we propose new kinds of DOEs which utilize superposition of different field distributions to allow more flexible functionality.

In the following sections, the simulation and the design methods for the DOEs are described. Two design concepts of DOEs are proposed which enable 3D surface measurements for opaque samples. The functionality and limitation of the DOEs are discussed based on the simulation results.

2 Diffraction simulation methods

To design such DOEs, one follows the procedures shown in Fig. 2.1 [HVS12]. First, a target field distribution is created, which is a spot array in this case. Then it propagates back through a certain working distance by simulation and the field distribution on the working plane of the DOE is obtained. In this case, the DOE is simply a piece of glass with micro structures etched on the surface. The structures are micro peaks and valleys, and they can control the phase of light to form a designed pattern. So only the phase of the field distribution is used, because a DOE made of pure glass can only control the phase of the field. Moreover, for manufacturing convenience, the phase is binarized because etching a binary profile on the glass is the easiest. The binarized phase then represents the micro peaks and valleys on the glass surface of the DOE. Finally, the binarized phase propagates again through the designed working distance by simulation to examine the produced spot array.

To make a DOE which can produce the same pattern as designed, the key in the above-mentioned procedures is to accurately calculate the field distribution after it propagates a certain distance. This is also the central problem for a diffraction simulation as Fig. 2.2 shows, where we want to calculate the field distribution $u(x, y, z)$ after the initial field at $z = 0$ propagates a certain distance through a medium with the refractive index n. Traditional geometrical optics methods like ray tracing are not able to simulate the diffraction phenomenon.

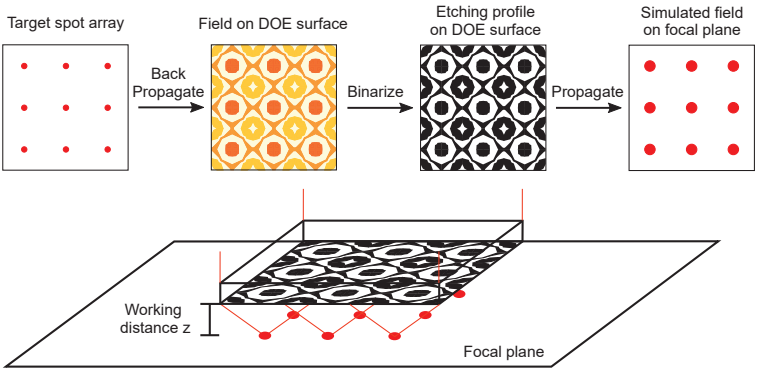

Figure 2.1: Design procedures of the DOE [HVS12]. The patterns are only for demonstration purpose and they are not generated by a real simulation.

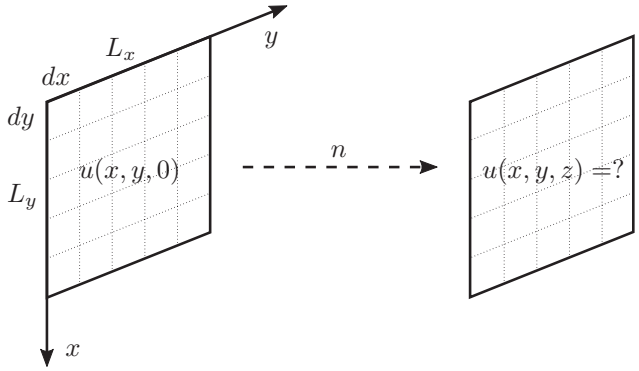

Figure 2.2: Calculating the field distribution after propagating a certain distance.

Meanwhile, full-wave solvers like FDTD or FEM can provide most accurate results by spatially discretizing Maxwell's equations in the computational domain. However, due to the huge size of the discretized grid for our 3D simulation scale in the millimeter range and the wavelength in the near-infrared spectrum, these methods would take months or years for a single run on normal servers even with GPU acceleration, which makes it inefficient for iterative design and optimization. So the classical diffraction theory in Fourier optics which uses scalar approximation for the Maxwell's equations is the suitable choice and now becomes the cornerstone for analysis of diffraction in wave optics [Voe11].

Generally, the propagation of light, which is identified as electromagnetic wave [Max65], is governed by Maxwell's equations:

$$\begin{cases} \dfrac{\partial \mathbf{D}}{\partial t} &= \nabla \times \mathbf{H}, \\ \dfrac{\partial \mathbf{B}}{\partial t} &= -\nabla \times \mathbf{E}, \\ \nabla \cdot \mathbf{B} &= 0, \\ \nabla \cdot \mathbf{D} &= 0. \end{cases}$$

With time-harmonic field and scalar approximation, Maxwell's equations are simplified into scalar Helmholtz's Equation [Goo05][KH14]:

$$\Delta u(\mathbf{r}, \omega) + k^2 u(\mathbf{r}, \omega) = \mathbf{0}, \tag{2.1}$$

where u is the scalar field of light which replaces $\mathbf{E}$ and $\mathbf{H}$ since they both satisfy the above equation, $\mathbf{r} = (x, y, z)$ is the coordinate, ω is the angular frequency of the light which we drop afterwards for simplicity since the frequency dependency is implicitly assumed, $k = 2\pi n/\lambda$ is the wave number where n is the refractive index of the medium and λ is the wavelength. The accuracy of the scalar approximation in diffraction is discussed in [Sil62][Lin72][BGG98]. They have shown that the scalar theory can yield sufficiently accurate results when the diffracting aperture size and observation distance from the aperture are both large compared to the wavelength, which is applicable in our case with the aperture size and the working distance in millimeter range.

Under the scalar approximation, there are two exact solutions for the scalar Helmholtz Equation (2.1) with the boundary condition on an opaque screen with finite apertures:

$$u(x, y, 0) = u_0(x, y), \tag{2.2a}$$

and the Sommerfeld radiation condition:

$$\lim_{|\mathbf{r}|\to\infty} |\mathbf{r}| \left(\frac{\partial u(\mathbf{r})}{\partial |\mathbf{r}|} - iku(\mathbf{r}) \right) = \mathbf{0}, \tag{2.2b}$$

which implies that the wave should decay when propagating to the infinity and no wave should be radiated back from the infinity.

With the boundary condition (2.2a) and (2.2b), one solution is known as the Rayleigh-Sommerfeld integral [Som96][Som04]:

$$u(\mathbf{r}) = \iint_{\mathbf{\Sigma}} u_{\mathrm{o}}(\mathbf{r}') \frac{e^{-ik|\mathbf{r}-\mathbf{r}'|} z}{|\mathbf{r}-\mathbf{r}'|^2} dx'dy', \tag{2.3}$$

where Σ denotes the surface on the boundary, i.e. the aperture plane and the semi-infinite sphere behind it, $\mathbf{r}' = (x', y', z')$ is the coordinate on Σ.

The other solution is the angular spectrum method [BRS50] as the following equation shows, which is also the simulation method used in [HVS12]:

$$u(\mathbf{r}) = \iint_{-\infty}^{\infty} U_{\mathrm{o}}(\alpha, \beta) e^{-i\gamma(\alpha,\beta)z} e^{-i(\alpha x+\beta y)} d\alpha d\beta, \tag{2.4}$$

where $U_0(\alpha, \beta) = \left(\frac{1}{2\pi}\right)^2 \iint_{-\infty}^{\infty} u_{\mathrm{o}}(x, y) e^{i(\alpha x+\beta y)} d\alpha d\beta$

is the Fourier transform of the initial field distribution at $z = 0$. α, β and $\gamma(\alpha, \beta)$ are called spatial frequencies which satisfy the relation $k^2 = \alpha^2 + \beta^2 + \gamma^2$. Equ. (2.4) implies that $u(\mathbf{r}) = u(x, y, z)$, which is the field distribution after $u_0(x, y) = u(x, y, 0)$ propagating a distance z, equals to the inverse Fourier transform of the product of $U_0(\alpha, \beta)$ and $e^{-i\gamma(\alpha,\beta)z}$.

Both solutions can solve the distribution of a field after propagating a defined distance as Fig. 2.2 shows. The angular spectrum method is in spatial frequency domain and the Rayleigh-Sommerfeld integral in real spatial domain. Analytically, they are equivalent and will provide the same simulation results. However, numerically they show different behaviour and are therefore suitable for solving different problems.

The reason is due to the sampling of these two integrals. Knowing the initial field distribution $u_0(x, y)$, we want to calculate the new field $u(x, y, z)$. Because analytic solutions of them are not known, they are calculated numerically. The first step is to discretize the initial field $u_0(x, y)$ as Fig. 2.2 shows.

For the Rayleigh-Sommerfeld integral in Eq. (2.3), the sampling is straightforward. If the initial field u_0 is discretized into smaller pieces, the sampling interval dx' and dy' also becomes smaller and the product inside the integral has a higher sampling rate. Generally, when the computational pixel size is smaller than a half of the wavelength, the integral is sufficiently well sampled [SW06].

However, for the angular spectrum method, the sampling is different due to the Fourier transform. As Eq. (2.4) shows, the angular spectrum method is the inverse Fourier transform of the product of $U_0(\alpha, \beta)$ and an oscillating phase $e^{-i\gamma(\alpha,\beta)z}$. This product has to be sampled sufficiently. On the one hand, $U_0(\alpha, \beta)$ is the Fourier transform of $u_0(x, y)$. So dx and dy need to be small enough to avoid aliasing in the frequency domain. On the other hand, $e^{-i\gamma(\alpha,\beta)z}$ will be sufficiently sampled when the phase of the oscillating term varies by less than π in each sampling step. This means that the sampling interval $d\alpha$ and $d\beta$ also has to be small enough to have a small variation step of $\gamma(\alpha, \beta)$. The size of $d\alpha$ and $d\beta$ is proportional to $1/L_x$ and $1/L_y$ in Fig. 2.2. This requires a computational window size which should be large enough to resolve $\gamma(\alpha, \beta)$. Besides, the propagation distance z should also be short enough.

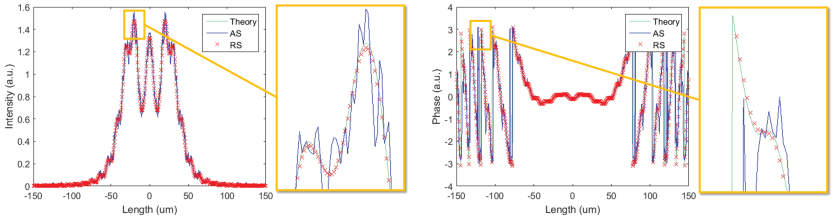

(a) Intensity of the fields after the slit. (b) Phase of the fields after the slit.

Figure 2.3: Simulation of the field distribution after a 1D slit by different methods.

These restrictions require a large computational window and small pixels simultaneously in certain cases. In our simulation scale, we have found that the angular spectrum method needs large zero padding which will lead to a large number of total computational pixels and a longer runtime.

Moreover, the angular spectrum method will have an implicit assumption of a periodic boundary condition due to the property of the discrete Fourier transform which needs to be treated carefully. The Rayleigh-Sommerfeld integral assumes zero boundary conditions which is easier to handle.

Fig. 2.3 shows the field distribution of a $100\,\mu\mathrm{m}$ 1D slit after propagating a distance of $1\,\mathrm{mm}$, which is a 2D simulation. The wavelength is $1\,\mu\mathrm{m}$. The total simulation length is $300\,\mu\mathrm{m}$. In such a simulation scale, we can see that the Rayleigh-Sommerfeld integral fits better with the theoretical result, while the angular spectrum method shows more oscillations and deviations. The detailed numerical implementation for the Rayleigh-Sommerfeld integral can be found in [SW06], and that for the angular spectrum method is almost identical to the common Fresnel diffraction implementation in [Voe11].

By the Rayleigh-Sommerfeld integral, we made a simulation with the computational window size $L_x = L_y = 2.4\,\mathrm{mm}$, the pixel size $dx = dy = 0.4\,\mu\mathrm{m}$ and the propagation distance $z = 1\,\mathrm{mm}$. The runtime for a single propagation is around $17\,\mathrm{s}$, which is sufficiently short for iterative design and optimization. Thus the Rayleigh-Sommerfeld integral is chosen as the simulation method in this work. All the DOE design in the following chapter is simulated by it.

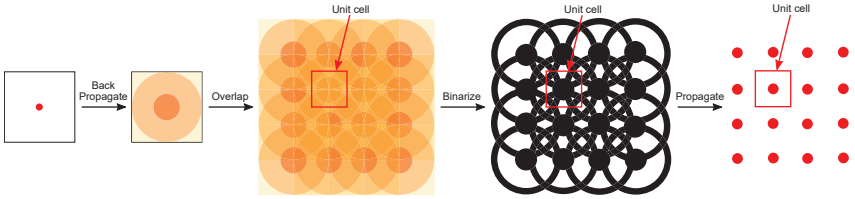

Figure 3.1: The DOE generates spot array with overlapping apertures. The patterns are only for demonstration purpose and they are not generated by a real simulation.

3 DOE Design for surface measurements

3.1 Overlapping apertures and multi-functional DOEs

To use the DOEs to replace high-NA objectives for fast scanning with high resolution, they need to be able to produce dense spot arrays with high-NA. This is achieved by the concept of overlapping apertures. As shown in Fig. 2.1, the spot array is produced by the DOE which is composed of periodic unit cells. However, a single spot in the array is not only produced by the unit cell right above it. It also receives contributions from all unit cells around the spot [HVS12]. This is equivalently explained by the design procedures in Fig. 3.1. The spot propagates back and forms a spherical-wave-like field distribution. In order to construct a spot array, this field is duplicated and overlapped with a certain pitch. Then the overlapping field is binarized and propagates back to verify the spot array which will be actually produced. In this case, the spot is not solely produced by the small unit cell above it, but it will be produced by the original spherical-wave-like field which is already overlapped with the adjacent ones. Thus, the NA of the spot is not limited by the pitch anymore. A dense spot array with high NA can be generated in this way.

However, as described in Section 1, such DOEs are not capable of measuring opaque objects. To improve the measurement capability of such DOEs in the current research, the key idea is the superposition of different field distributions. By simply adding different fields generated from different target light distributions, all the target patterns can be generated with one single DOE [DZXL03]. Such kind of DOEs is known as the multi-functional DOEs.

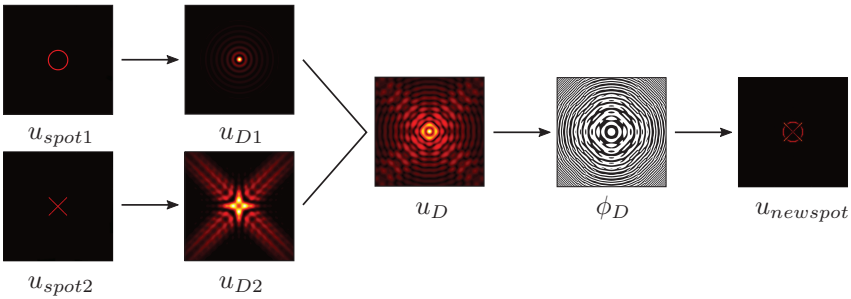

Figure 3.2: Design procedures for multi-functional DOEs.

For example, if one DOE can generate a circle and another one can generate a cross, the combined DOE of the previous two DOEs can generate a circle and a cross at the same time. Fig. 3.2 demonstrates the design procedures and simulation results for this DOE. u_{spot1} and u_{spot2} are the field distributions of a circle and a cross. u_{D1} and u_{D2} are the field distributions on the the working plane after u_{spot1} and u_{spot2} propagate back a certain working distance respectively. Then they are simply added together with a weight factor W and form a new field distribution:

$$u_D(x,y) = u_{D1}(x,y) + W u_{D2}(x,y). \tag{3.1}$$

Afterwards, the phase of u_D is extracted and binarized into ϕ_D with a binarization factor B [HVS12]:

$$\phi_D(x,y) = \mod\left(\left\lfloor \frac{\arg[u_D(x,y)] + B}{\pi} \right\rfloor, 2\right)\pi. \tag{3.2}$$

Finally, with plane-wave illumination, the binary DOE forms a field distribution e^{ϕ_D} and it propagates to the focal plane to show the actual pattern $u_{newspot}$, which in this case is the superposition of a circle and a cross. With this method, a single piece of a DOE can have a more flexible functionality. In the following sections, two DOE designs will be introduced to overcome the shortcomings of the previous DOEs in Fig. 2.1 for confocal microscopy. These designs utilize the idea of superposition to realize see-through and direct-imaging functions and are both able to measure opaque surfaces.

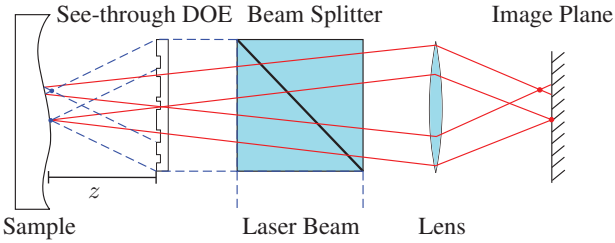

Figure 3.3: See-through configuration of a DOE-based confocal surface measurement system.

3.2 See-through DOE design

In order to illuminate and image the sample on the same side for confocal surface measurements, the spots need be able to be seen through the DOE without too much disturbance.

Fig. 3.3 shows a DOE-based multi-spot scanning confocal microscope for surface measurements. The dashed blue lines represent the illumination light and the solid red lines represent the light refelcted from the sample. The DOE generates high-NA spots which are imaged by a low-NA objective lens. In this way, although the low-NA lens will produce large spots on the image plane, the lateral resolution is still governed by the high-NA illumination spots, which is similar to the principle of super-resolution microscopy like STED or PALM [HW94][BPS$^+$06]. Meanwhile, a low-NA lens can offer a large field of view. Thus high resolution and large-area scanning can be achieved at the same time.

Fig. 3.4 shows a section of the simulated image for a 21×21 spot array with a pitch of $20\,\mu\mathrm{m}$, which is generated by a DOE with an NA of 0.7 and imaged by a lens with an NA of 0.2. The wavelength for the simulation is $785\,\mathrm{nm}$ The DOE multi-spot illuminator is designed in the similarly to the procedures described in [HVS12].

It is obvious that the spots are severely disturbed when they are imaged through the DOE. We are going to define an intensity contrast factor (ICF). The definition of it is going to be the ratio between the intensity of the central pixel on the image and the average intensity of the following unit cell:

$$\mathrm{ICF} = \frac{I_{center}}{I_{mean}}.$$

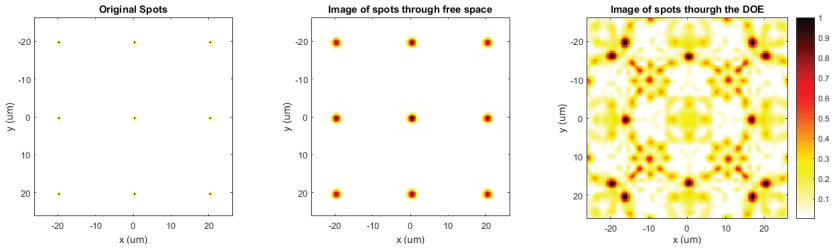

(a) 3×3 grid section in a 21×21 spot array.

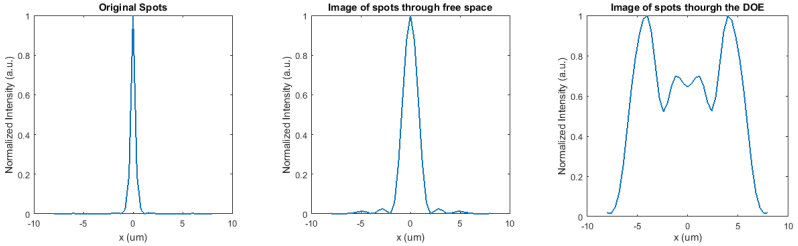

(b) Cross section of the intensity profile near central spot at $y = 0$.

Figure 3.4: Simulation of spots generated and imaged through a pure DOE illuminator.

In the ideal case, when a perfect spot array is imaged by such a configuration, the ideal ICF $= 116.38$. For the simulation in Fig. 3.4, we get the ICF $= 1.97$. As clearly shown in the very noisy picture, such DOEs are not capable for surface measurements when illumination and imaging systems are on the same side of the sample.

To reduce the disturbance added by the DOE itself, a plane-wave component is added to the original DOE. This is simply done as described in Section 3.1 by putting $u_{D2}(x, y) = 1$ as plane wave into Eq. (3.1):

$$u_D(x, y) = u_{D1}(x, y) + W,$$

where u_{D1} is the field distribution to produce a spot array like Fig. 2.1. In this way, the new DOE can not only generate a spot array, but also act as a transparent piece of glass which lets the low-NA objective to image the spots through it without too much disturbance. The simulation results of such a DOE is shown in Fig. 3.5 for a spot array with the same wavelength, spot number, pitch and NA as Fig. 3.4. The DOE is optimized iteratively with the working distance $z = 1.095\,\mathrm{mm}$, the weight

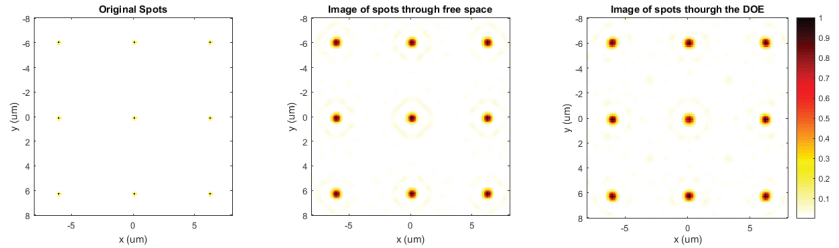

(a) 3×3 grid section in a 21×21 spot array.

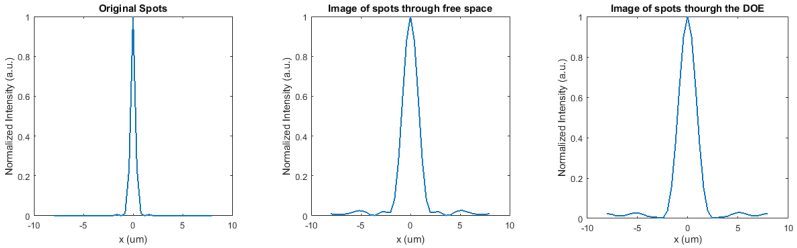

(b) Cross section of the intensity profile near central spot at $y = 0$.

Figure 3.5: Simulation of spots generated and imaged through a see-through DOE with a plane-wave component.

factor $W = 18$ and the binarization factor $B = 0.49\pi$ in Eq. (3.2) to achieve the highest intensities in the spot centers. Compared to the image simulation of the previous DOE, it is obvious that the spots are much less disturbed and can be clearly imaged by the low-NA objective with a highly improved ICF $= 48.25$.

Such DOEs can realize the concept of combining high-NA illumination and low-NA imaging for confocal surface measurements, which achieves high lateral resolution and large-area scanning. However, such configuration cannot significantly improve the axial resolution for 3D surface measurements. The reason can be derived from the image formation theory of scanning microscopes in Fig. 3.6. The field distribution $U(x_2, y_2)$ on the image plane according to the scanning position can be represented as:

$$U(x_2, y_2; x_s, y_s) \tag{3.3}$$
$$= \iint_{-\infty}^{\infty} h_1(x_0, y_0) t(x_0 - x_s, y_0 - y_s) h_2\left(\frac{x_2}{M} - x_0, \frac{y_2}{M} - y_0\right) dx_0 dy_0,$$

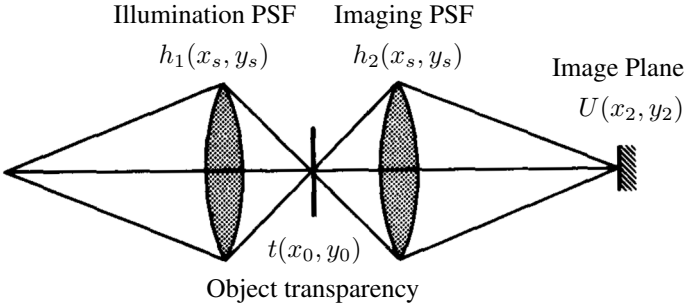

Figure 3.6: Optical configuration for a scanning microscope [WS84].

where (x_0, y_0) is the object coordinate, (x_2, y_2) is the image coordinate, (x_s, y_s) is the scanning position, $h_1(x_s, y_s)$ is the illumination point spread function (PSF), $h_2(x_s, y_s)$ is the imaging PSF, and $t(x_0, y_0)$ is the object transparency as shown in Fig. 3.6.

For a point object, the object transparency is $t(x_0, y_0) = \delta(x_0, y_0)$, and Eq. (3.3) can be simplified into:

$$\begin{aligned} & U(x_2, y_2; x_s, y_s) \\ &= \iint_{-\infty}^{\infty} h_1(x_0, y_0)\delta(x_0 - x_s, y_0 - y_s)h_2\left(\frac{x_2}{M} - x_0, \frac{y_2}{M} - y_0\right) dx_0 dy_0 \\ &= h_1(x_s, y_s)h_2\left(\frac{x_2}{M} - x_s, \frac{y_2}{M} - y_s\right). \end{aligned} \tag{3.4}$$

For a plane object, e.g. a mirror, the object transparency is equivalent to $t(x, y) = 1$, and Eq. (3.3) can be simplified into:

$$\begin{aligned} & U(x_2, y_2; x_s, y_s) \\ &= \iint_{-\infty}^{\infty} h_1(x_0, y_0)h_2\left(\frac{x_2}{M} - x_0, \frac{y_2}{M} - y_0\right) dx_0 dy_0 \\ &= h_1(x_2, y_2) * h_2(x_2, y_2). \end{aligned} \tag{3.5}$$

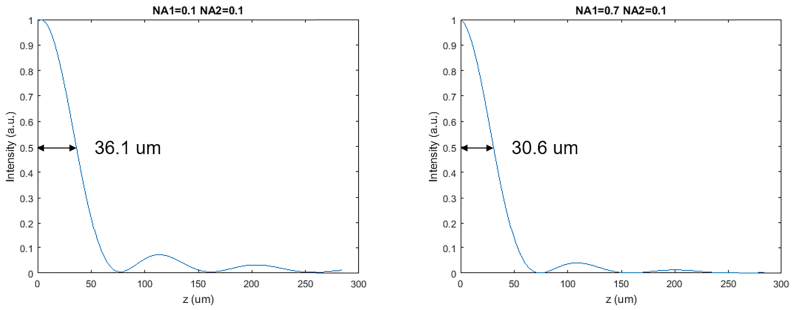

(a) Low-NA illumination and low-NA imaging.

(b) High-NA illumination and low-NA imaging.

Figure 3.7: Axial intensity responses of confocal systems for a plane object.

From Eq. (3.4) and Eq. (3.5), it is clearly shown that for a point object the response on the image plane is the product of the illumination and the imaging PSFs, while for a plane object the image is the convolution of the two PSFs. In our optical configuration with high-NA illumination and low-NA imaging, this means that for a point object, the response on the image plane will be governed by the high-NA PSF; for a plane object, it will be governed by the low-NA PSF. Thus for the 3D surface measurement, which is similar to a plane, the axial resolution cannot benefit from the high-NA illumination.

Fig. 3.7 shows simulations of axial intensity responses of confocal microscope systems for a plane object with both low-NA illumination and imaging, and with high-NA illumination and low-NA imaging respectively. The simulation setup is very simple. A spot on a mirror which is produced by an illumination lens is imaged by an imaging lens. Then the mirror is gradually moved away from the focal point and the intensity of the central pixel in the image is recorded. For both low-NA illumination and imaging, the axial half width half maximum (HWHM) is $36\,\mu\mathrm{m}$. And with a high-NA illumination, the axial HWHM is around $30\,\mu\mathrm{m}$. Although there is an improvement, it is not very significant and impressive.

In conclusion, such configuration in Fig. 3.3 can improve the lateral resolution by the high-NA spots produced by the DOE. However, the axial resolution is still strongly restricted by the low-NA objective. Thus it is not very suitable for 3D surface measurements.

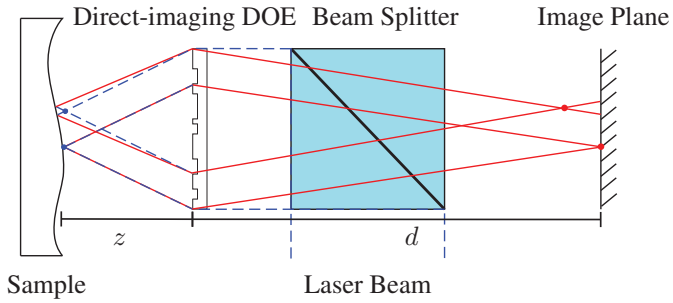

Figure 3.8: Direct-imaging configuration of a DOE-based confocal surface measurement system.

3.3 Direct-imaging DOE design

In order to increase the axial resolution and make the DOE suitable for 3D surface measurements, the optical configuration for the direct-imaging DOE design is proposed as Fig. 3.8. In this case, the DOE is the superposition of two kinds of lenses with overlapping apertures. One acts as an illumination lens which converts an incident plane wave into a spot array. The other one acts as the imaging lenses which directly image the spots onto the imaging sensor. The two lenses are overlapped as Fig. 3.1 shows. The field distribution for the new DOE is calculated again according to Eq. (3.1):

$$u_D = u_{lens1} + W u_{lens2}.$$

In this way the illumination and the imaging are both high-NA and the system can have the same performance as a high-NA confocal microscope.

Fig. 3.10 shows the simulation results with the setup in Fig. 3.8. The dashed blue lines represent the illumination light and the solid red lines represent the light refelcted from the sample. The spots are generated by the direct-imaging DOE and again imaged by itself onto the image plane. It is again optimized iteratively to achieve the highest intensities in the spot centers with the working distance $z = 1.11\,\mathrm{mm}$, the distance from the DOE to the image sensor $d = 21.262\,\mathrm{mm}$, the weighting factor $W = 0.045$ and the binarization factor $B = 0.97\pi$ in Eq. (3.2).

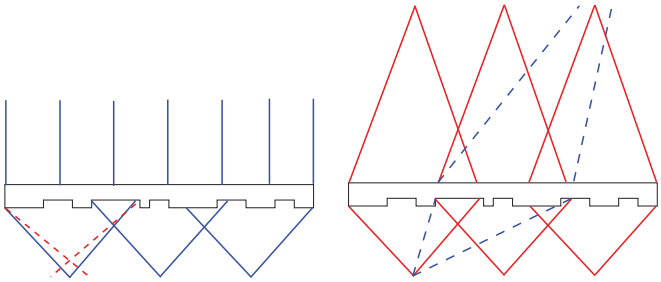

(a) Illumination through the superimposed lens

(b) Imaging through the adjacent lens.

Figure 3.9: Side effects which cause irregular interference patterns.

The pitch is $100\,\mu\mathrm{m}$ and the simulation wavelength is $785\,\mathrm{nm}$. Different numbers of spots are created for the simulation. For a perfect spot on the image plane in this configuration, we calculate an ICF $= 267.79$. Fig. 3.10 shows a 5×5 spot array. The spots can still be seen with an ICF $= 38.86$. However, irregular interference patterns can already be observed in the image. When the number of spots further increases, the interference patterns will become more and more significant as in Fig. 3.10 with ICF $= 19.72$ and Fig. 3.10 with ICF $= 5.08$. The ICF drops with the increase of spot numbers. Eventually, the spots are covered by the interference patterns and they cannot be distinguished any more on the image.

These interference patterns are mainly caused by the side effects of superposition of different DOEs and overlapping apertures. As mentioned previously, the DOE is composed of two components which are generally two kinds of lenses with different focal lengths. They act as the illumination lenses and imaging lenses respectively. However, they will not work separately as we want for illumination and imaging. They will always take effect at the same time. When projecting the illumination spots, the imaging lenses will also produce a blurred spot around the spot we need, which is shown as Fig. 3.9.

Besides, on the imaging side, due to the overlapping apertures, one spot will not only pass the designed lens to form a spot on the image sensor, but also it will go through the adjacent lenses to form other blurred spots which add some disturbances to the image, which is shown in Fig. 3.9. As the number of spots increases, the image quality will reduce.

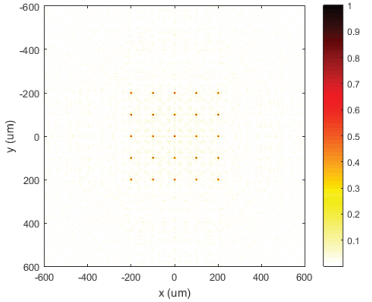

(a) 5×5 spot array on the image.

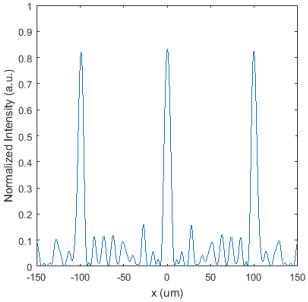

(b) Cross section at $y = 0$ in the 5×5 spot array.

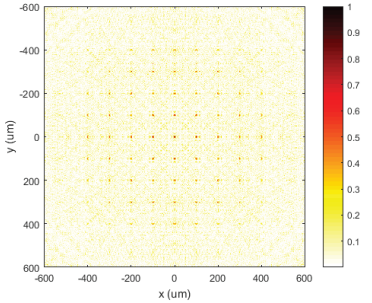

(c) 9×9 spot array on the image.

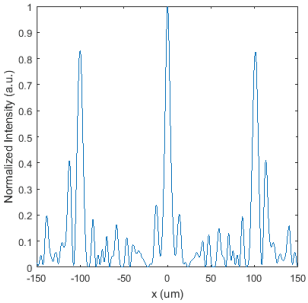

(d) Cross section at $y = 0$ in the 9×9 spot array.

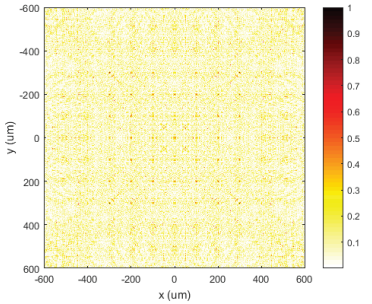

(e) 11×11 spot array on the image.

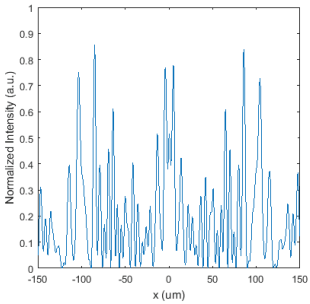

(f) Cross section at $y = 0$ in the 11×11 spot array.

Figure 3.10: Simulation of the field intensity on the image plane for the direct-imaging DOE design.

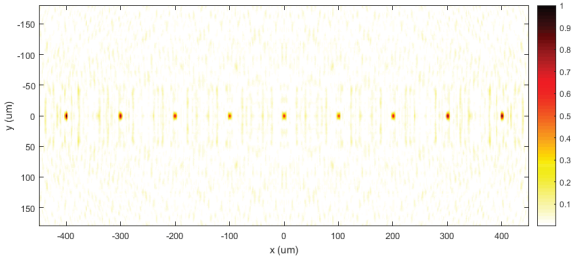

(a) The central 9 spots in a line with 21 spots on the image plane.

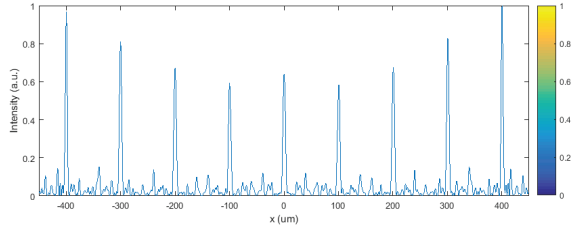

(b) Cross section of intensity profile of the line at $y = 0$.

Figure 3.11: Simulation of a spot line produced by the direct-imaging DOE.

The reason behind these side effects is too much overlapping of the elements. The overlapping can be reduced by decreasing the working distance, decreasing the NA, or increasing the pitch of the elements. However, none of these is desirable for 3D measurement. Because larger working distance, higher NA and smaller pitch are required for faster and more accurate measurement.

One possible solution could be using a line of spots instead of a 2D array to reduce the overlapping. In this case, there is no longer interference from the top and bottom spots. Meanwhile, one spot will receive less disturbances from the spots farther away. Thus the overall disturbances for a single spot can be reduced to an acceptable level and the line of spots can be extended infinitely. Fig. 3.11 shows a line of 21 spots with the working distance $z = 1.11\,\mathrm{mm}$, the distance from the DOE to the image sensor $d = 21.262\,\mathrm{mm}$, the weighting factor $W = 0.065$ and the binarization factor $B = 0.97\pi$ in Eq. (3.2). The pitch is $100\,\mu\mathrm{m}$ and the simulation wavelength is $785\,\mathrm{nm}$. As shown in the picture, the center spot

receives the most disturbances from other spots but it is still clearly visible with an ICF $= 32.53$. And even with the increase of the spots, the central spot will receive less disturbance from the unit cells which is far away , which implies that the concept works theoretically in the simulation.

In conclusion, two DOE design concepts are proposed in this chapter. They can both produce illumination spots with an NA of 0.7 by simulation. The first see-through DOE design provides better intensity contrast with an ICF $= 48.25$ compared to an ideal ICF $= 116.38$, but it is only capable of 2D measurements. The second direct-imaging design is able to measure 3D surfaces but the number of spots is highly limited due to severe interference caused by overlapping of the components. A line scanner could be a potential solution to control the interference to an acceptable level with an ICF $= 32.53$ compared to an ICF $= 267.79$ in the ideal configuration.

4 Summary

In the current research, DOEs are used to replace high NA objectives in confocal microscopy. However, they can only measure semi-transparent samples. In this work, the ideal of superposition are proposed to overcome this limit and to enable the application of DOE for opaque surface measurements. Different methods to simulate light diffraction are compared for design the DOE. Two different DOE design concepts are simulated and investigated. Both concepts can produce an illumination spot array with an NA of 0.7. The first see-through design has a good intensity contrast on the image but it cannot provide good axial resolution. The second direct-imaging design has the same depth discerning capability as the traditional confocal microscopy. However, it suffers from low intensity contrast due to overlapping of different wave component. 1D arrangement of the spots as a line is proposed to reduce the interference and it has the potential in real industrial application.

The first piece of DOE prototype is already produced and ready for testing. In the future, experiments with the prototype will be performed to verify the simulation results, and new possibilities to use structured illumination and interference with DOEs will be investigated for 3D measurement.

Bibliography

[BGG98] Jon M Bendickson, Elias N Glytsis, and Thomas K Gaylord. Scalar integral diffraction methods: unification, accuracy, and comparison with a rigorous boundary element method with application to diffractive cylindrical lenses. *JOSA A*, 15(7):1822–1837, 1998.

[BPS+06] Eric Betzig, George H Patterson, Rachid Sougrat, O Wolf Lindwasser, Scott Olenych, Juan S Bonifacino, Michael W Davidson, Jennifer Lippincott-Schwartz, and Harald F Hess. Imaging intracellular fluorescent proteins at nanometer resolution. *Science*, 313(5793):1642–1645, 2006.

[BRS50] Henry George Booker, JA Ratcliffe, and DH Shinn. Diffraction from an irregular screen with applications to ionospheric problems. *Phil. Trans. R. Soc. Lond. A*, 242(856):579–607, 1950.

[DSS+09] Michael E. Dailey, Sidney L. Shaw, Jason R. Swedlow, Matthias F. Langhorst, and Michael W. Davidson. Microscopy techniques for live-cell imaging. `http://zeiss-campus.magnet.fsu.edu/articles/livecellimaging/techniques.html`, 2009. Online; accessed 3-November-2017.

[DZXL03] Enwen Dai, Changhe Zhou, Peng Xi, and Liren Liu. Multifunctional double-layered diffractive optical element. *Optics letters*, 28(17):1513–1515, 2003.

[Goo05] Joseph W Goodman. *Introduction to Fourier optics*. Roberts and Company Publishers, 2005.

[HVS12] Bas Hulsken, Dirk Vossen, and Sjoerd Stallinga. High NA diffractive array illuminators and application in a multi-spot scanning microscope. *Journal of the European Optical Society - Rapid publications*, 7, 2012.

[HW94] Stefan W Hell and Jan Wichmann. Breaking the diffraction resolution limit by stimulated emission: stimulated-emission-depletion fluorescence microscopy. *Optics letters*, 19(11):780–782, 1994.

[KH14] Andreas Kirsch and Frank Hettlich. *The Mathematical Theory of Maxwell's Equations*. Karlsruhe Institute of Technology (KIT), 2014.

[LB14] Xiyuan Liu and Karl-Heinz Brenner. High resolution wavefront measurement with phase retrieval using a diffractive overlapping micro lens array. In *Fringe 2013*, pages 233–236. Springer, 2014.

[Lin72] Burn Jeng Lin. Electromagnetic near-field diffraction of a medium slit. *JOSA*, 62(8):976–981, 1972.

[LSB12] Xiyuan Liu, Tim Stenau, and Karl-Heinz Brenner. Diffractive micro lens arrays with overlapping apertures. In *Information Optics (WIO), 2012 11th Euro-American Workshop on*, pages 1–2. IEEE, 2012.

[Max65] James Clerk Maxwell. A dynamical theory of the electromagnetic field. *Philosophical transactions of the Royal Society of London*, 155:459–512, 1865.

[Sil62] Samuel Silver. Microwave aperture antennas and diffraction theory. *JOSA*, 52(2):131–139, 1962.

[Som96] Arnold Sommerfeld. Mathematische theorie der diffraction. *Mathematische Annalen*, 47(2):317–374, 1896.

[Som04] Arnold Sommerfeld. *Mathematical Theory of Diffraction*. Birkhäuser Boston, Boston, MA, 2004.

[SW06] Fabin Shen and Anbo Wang. Fast-fourier-transform based numerical integration method for the rayleigh-sommerfeld diffraction formula. *Applied optics*, 45(6):1102–1110, 2006.

[VBR+15] Jeroen Vangindertael, Isabel Beets, Susana Rocha, Peter Dedecker, Liliane Schoofs, Karen Vanhoorelbeke, Johan Hofkens, and Hideaki Mizuno. Super-resolution mapping of glutamate receptors in c. elegans by confocal correlated palm. *Scientific reports*, 5:13532, 2015.

[Voe11] David George Voelz. *Computational fourier optics: a MATLAB tutorial*. SPIE press Bellingham, WA, 2011.

[WS84] Tony Wilson and Colin Sheppard. *Theory and practice of scanning optical microscopy*, volume 180. Academic Press London, 1984.

[Zhe16] Guoan Zheng. *Fourier Ptychographic Imaging: A Matlab Tutorial*. Morgan & Claypool Publishers, 2016.